

## ABSTRACT

Title of dissertation:      Measuring topology of BECs  
in a synthetic dimensions lattice

Dina Genkina  
Doctor of Philosophy, 2018

Dissertation directed by:   Professor Ian Spielman  
Department of Physics

Measuring topology of BECs in a synthetic dimensions lattice

by

Dina Genkina

Dissertation submitted to the Faculty of the Graduate School of the  
University of Maryland, College Park in partial fulfillment  
of the requirements for the degree of  
Doctor of Philosophy  
2018

Advisory Committee:  
Professor Ian Spielman, Chair/Advisor

© Copyright by  
Dina Genkina  
2018



## Chapter 4: Synthetic dimensional lattice

In this chapter we explain the idea of an effective 2-D lattice with one real dimension created by lattice sites of a 1-D optical lattice and one 'synthetic' dimension created by treating the internal spin states of the atom as sites along a transverse axis. We do this by treating each dimension individually first. In the section [4.1](#), we describe 1-D optical lattices. We explain the far off resonant interaction that leads to the AC Stark shift, and use it to write down the 1-D optical lattice Hamiltonian. We describe the often used tight binding approximation of the lattice Hamiltonian. We describe how the lattice is calibrated in our lab, and introduce Bloch oscillations.

In section [4.2](#), we describe the hyperfine structure of Rubidium, used as sites in the 'synthetic' dimension. We then describe two methods for coupling them to introduce tunneling in the synthetic dimensions: rf and Raman transitions. We describe the calibration procedures, and show ground states of the system with each of the couplings applied. In the last section, we combine the two dimensions and write out the full synthetic dimensions Hamiltonian. We plot the band structure, and describe the emergence of the effective magnetic field. We show the calibration procedure, and show the ground states of the system, featuring both bulk and edge states with narrowing due to the magnetic length. We then show skipping orbits created by loading a superposition of states on the edge of the system, analogous to edge magnetoplasmons. The experiments in this section were detailed in the publication [\[1\]](#).

## 4.1 One dimensional optical lattices

The first, 'real' dimension in the synthetic dimensional lattice is discretized into sites by an optical lattice. Optical lattices are a staple of cold atomic physics, and are commonly used to emulate the crystal structure present in metals and other condensed matter systems. In this section, we describe the origin of the periodic potential, derive the Hamiltonian and show how the lattice depth is detected and calibrated in the lab.

### 4.1.1 Far off-resonant atom-light interaction

As described in section ??, on timescales where spontaneous emission can be neglected, two-level atoms exposed to laser radiation undergo coherent Rabi oscillations between the two levels. Starting with  $c_g$  and  $c_e$  as the time-dependent coefficients multiplying the eigenstate wavefunctions of the ground and excited state respectively, and assuming the atom starts in the ground state  $c_g(t=0) = 1$ , we make the traditional transformation to the rotating frame:

$$c'_g(t) = c_g(t) \tag{4.1}$$

$$c'_e(t) = c_e(t)e^{-i\delta t}, \tag{4.2}$$

where  $\delta$  is the detuning of laser light from resonance. In this frame, we can write the atom-light Hamiltonian in the  $\begin{pmatrix} c'_g \\ c'_e \end{pmatrix}$  basis as:

$$H = \hbar \begin{pmatrix} -\delta/2 & \Omega/2 \\ \Omega/2 & \delta/2 \end{pmatrix}, \tag{4.3}$$

where  $\Omega$  is the coupling strength, also known as the Rabi frequency. In the limit of no coupling,  $\Omega = 0$ , in the rotating frame the eigenenergies are  $E_{\pm} = \pm\hbar\delta/2$ . For non-zero coupling, finding the eigenvalues of  $H$  gives  $E_{\pm} = \pm\hbar\sqrt{\delta^2 + \Omega^2}/2$ . Therefore, the bare (without light) eigenenergies are shifted in the presence of the light.

For a far detuned laser beam, one expects that no absorption of the light will actually take place, and the atom will remain entirely in the ground state. Indeed, solving the Shroedinger equation with the above Hamiltonian

$$i\hbar \frac{d}{dt} \begin{pmatrix} c'_g \\ c'_e \end{pmatrix} = H \begin{pmatrix} c'_g \\ c'_e \end{pmatrix} \quad (4.4)$$

we obtain the oscillating excited state population

$$c'_e(t) = -i \frac{\Omega}{\sqrt{\Omega^2 + \delta^2}} \sin \left( \frac{\sqrt{\Omega^2 + \delta^2} t}{2} \right), \quad (4.5)$$

where the amplitude of the oscillation approaches zero in the limit  $\Omega \ll \delta$ . Thus, the only effect of the light in this regime is to shift the eigenenergies of the ground and excited states. Expanding the energies in the small parameter  $\Omega/\delta$ , we obtain the shifted energies  $E_{\pm} = \pm\hbar\sqrt{\delta^2 + \Omega^2}/2 \approx \pm(\delta/2 + \Omega^2/4\delta)$ . The shift from bare energy levels is thus

$$\Delta E_{\pm} = \pm\Omega^2/4\delta. \quad (4.6)$$

This laser intensity dependent energy shift is called the AC Stark shift, and is the basis of most laser created potentials for cold atoms.

For the ground state, and a red detuned laser beam (where the laser frequency is lower than the resonant frequency), this creates energy minima in locations of maximal laser intensity. For the lattice described in this chapter, as well as for the trapping of our atoms in the final stages of cooling, we use high power (up to 10 W)

lasers with wavelength  $\lambda_L = 1064$  nm.

#### 4.1.2 Lattice Hamiltonian

Our 1-D optical lattice is created by retro-reflecting the  $\lambda_L = 1064$  nm laser, creating a standing wave of light. Via the AC Stark shift, this creates a periodic potential for the atoms of the form

$$V = V_0 \sin^2(k_L x), \quad (4.7)$$

where  $k_L = 2\pi/\lambda_L$  is the wavenumber associated with the lattice recoil momentum.

The time-independent Hamiltonian, for some eigenenergy  $E_n$ , will be given by

$$-\frac{\hbar^2}{2m} \frac{d^2}{dx^2} \Psi_n(x) + V_0 \sin^2(k_L x) \Psi_n(x) = E_n \Psi_n(x). \quad (4.8)$$

Since the potential is spatially periodic, we can invoke Bloch's theorem [2]:

$$\Psi_{n,q} = e^{iqx} u_{n,q}(x), \quad (4.9)$$

where  $q$  is the crystal momentum restricted to  $\pm \hbar k_L$ , and  $u_{n,q}(x)$  is the spatially varying part of the wavefunction. Plugging this in to the Hamiltonian, we obtain

$$-\frac{\hbar^2}{2m} \left( -q^2 + 2iq \frac{d}{dx} + \frac{d^2}{dx^2} \right) u_{n,q}(x) + V_0 \sin^2(k_L x) u_{n,q}(x) = E_n u_{n,q}(x). \quad (4.10)$$

Expanding  $u_{n,q}(x)$  in Fourier components commensurate with the lattice period of  $2k_L$  as  $u_{n,q}(x) = \sum_{j=-\infty}^{\infty} a_j e^{i2k_L j x}$ , we obtain

$$\sum_j \left( \frac{\hbar^2}{2m} (q + 2k_L)^2 a_j + V_0 \sin^2(k_L x) a_j \right) e^{i2k_L j x} = E_n \sum_j a_j e^{i2k_L j x}. \quad (4.11)$$



Re-writing  $\sin^2(k_L x) = (e^{-2ik_L x} + e^{2ik_L x} - 2)/4$ , multiplying both sides by  $e^{i2k_L j' x}$  and invoking  $\sum c_j e^{ik(j-j')} = \delta_{jj'}$ , where  $\delta_{jj'}$  is the Kroniker delta and  $c_j$  are appropriately normalized coefficients, we get for any value of the index  $j$

$$\frac{\hbar^2}{2m}(q + 2k_L j)^2 a_j - \frac{V_0}{4}(a_{j+1} + a_{j-1}) = E_n a_j. \quad (4.12)$$

This can be expressed in matrix form

$$H_L = \begin{pmatrix} \ddots & & & & & \\ & \frac{\hbar^2}{2m}(q + 4k_L)^2 & \frac{V_0}{4} & 0 & 0 & 0 \\ & \frac{V_0}{4} & \frac{\hbar^2}{2m}(q + 2k_L)^2 & \frac{V_0}{4} & 0 & 0 \\ & 0 & \frac{V_0}{4} & \frac{\hbar^2}{2m}q^2 & \frac{V_0}{4} & 0 \\ & 0 & 0 & \frac{V_0}{4} & \frac{\hbar^2}{2m}(q - 2k_L)^2 & \frac{V_0}{4} \\ & & 0 & 0 & \frac{V_0}{4} & \frac{\hbar^2}{2m}(q - 4k_L)^2 \\ & & & & & \ddots \end{pmatrix}, \quad (4.13)$$

in the basis of momentum orders  $|k\rangle = e^{ikx}$  given by:

$$\begin{pmatrix} \vdots \\ |q + 4k_L\rangle \\ |q + 2k_L\rangle \\ |q\rangle \\ |q - 2k_L\rangle \\ |q - 4k_L\rangle \\ \vdots \end{pmatrix}. \quad (4.14)$$

This matrix can be diagonalized for every value of the crystal momentum  $q$ , with the resulting band structure shown in Figure 1. It is convenient to define the lattice recoil energy  $E_L = \hbar^2 k_L^2 / 2m$ . Then, we can re-write the Hamiltonian with

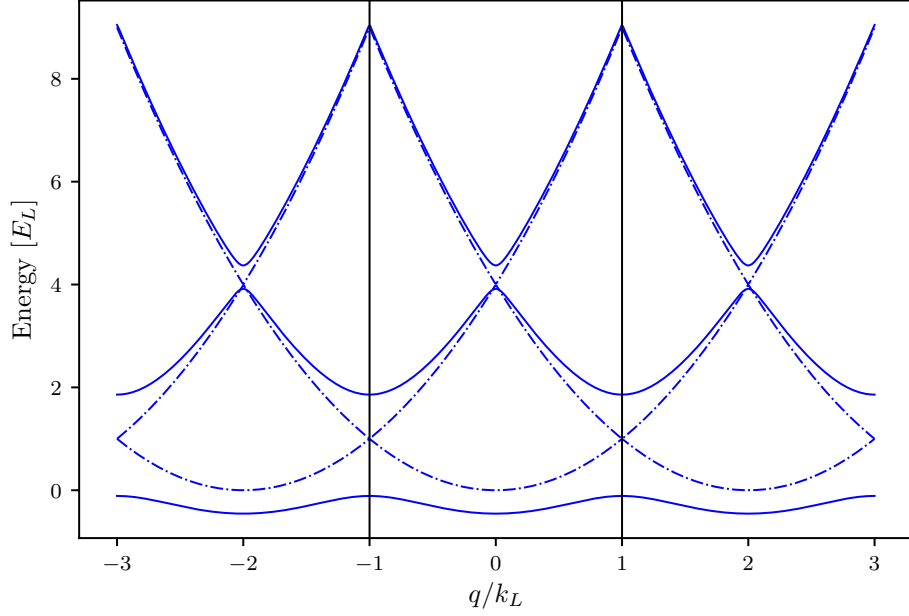


Figure 1: Lattice band structure in the extended zone scheme. The dashed lines represent the limit of zero lattice depth, with the regular parabolic dispersion relation of a free particle repeating with reciprocal lattice period. The solid lines are the dispersion relation at  $V_0 = 4.0 E_L$ , showing the opening of gaps at crossings of the zero lattice depth bands. The black lines demarcate the first Brillouin zone.

$V_0$  in units of  $E_L$  and momenta  $q$  in units of  $k_L$  as

$$H_L/E_L = \begin{pmatrix} \ddots & & & & & \\ & (q+4)^2 & \frac{V_0}{4} & 0 & 0 & 0 \\ & \frac{V_0}{4} & (q+2)^2 & \frac{V_0}{4} & 0 & 0 \\ & 0 & \frac{V_0}{4} & q^2 & \frac{V_0}{4} & 0 \\ & 0 & 0 & \frac{V_0}{4} & (q-2)^2 & \frac{V_0}{4} \\ & & 0 & 0 & \frac{V_0}{4} & (q-4)^2 \\ & & & & & \ddots \end{pmatrix}. \quad (4.15)$$

In any numerical simulation, the number of momentum orders that can be included is finite. We determine the value of the parameter  $n = \max(|j|)$  as the

lowest  $n$  at which the eigenvalues stop changing to machine precision from  $n - 1$ . The code for finding and plotting the eigenvalues and eigenvectors of the lattice hamiltonian is included in Appendix [MAKE APPENDIX WITH CODE?].

### 4.1.3 Tight binding approximation

In the limit of large lattice depths,  $V_0 > \approx 5E_L$ , the lattice Hamiltonian is well approximated by the tight-binding model. In the tight binding model, the basis is assumed to be a set of orthogonal functions, called Wannier functions, localized to each lattice site  $|j\rangle$ . The approximation lies in assuming only nearest neighbor tunnelings between the sites, forming the tight-binding Hamiltonian

$$H_{\text{tb}} = -t |j\rangle \langle j+1| + \text{H.c.}, \quad (4.16)$$

where  $t$  is the tunneling amplitude between nearest neighbor sites and H.c. stands for Hermitian conjugate. We have neglected the diagonal kinetic energy term, as it will be equal for every Wannier function  $|j\rangle$  and thus represents a constant energy offset. All the information about the lattice depth is therefore reflected in the tunneling amplitude  $t$ .

The tight binding Hamiltonian can also be expressed in the momentum basis by Fourier transforming the basis functions:

$$|j\rangle = \frac{1}{\sqrt{N}} \sum_{k_j} e^{-ik_j j} |k_j\rangle, \quad (4.17)$$

giving the Hamiltonian

$$H_{\text{tb}} = -\frac{1}{N} \sum_{k_1} \sum_{k_2} k_2 t e^{-ik_1} e^{ik_2(j+1)} |k_1\rangle \langle k_2| + \text{H.c} = 2t \cos(k) |k\rangle \langle k|. \quad (4.18)$$

From this we can directly read off the band structure of the tight binding Hamilto-

nian. First, we notice that we only obtain one band - to approximate higher bands with the tight binding approximation we would need to construct a different set of Wannier functions and a different tunneling strength. Second, we see that the lowest band is simply a cosine - therefore we have solved for the band structure without even defining what the basis Wannier functions are! Third, the amplitude of the cosine function is given by the tunneling strength  $t$ . This gives us a good clue as to how to determine the appropriate tunneling given a lattice depth  $V_0$  - simply find a  $t$  that matches the amplitude of the lowest band, which becomes cosinusoidal in the deep lattice limit.

The precise form of the Wannier functions depends on both the depth of the lattice and the band being reproduced. It is not necessary for us to find their full expression, as the band structure can be calculated without them. The definition, however, is

$$|j\rangle = \int_{\text{BZ}} e^{i\phi(q)-iqja} \Psi_q(x) dq, \quad (4.19)$$

where the integral is over the Brillouin zone, from  $-k_L$  to  $k_L$ ,  $a$  is the lattice spacing  $\lambda_L/2$ , and  $\Psi_q$  is the Bloch wavefunction at crystal momentum  $q$ , and  $\phi(q)$  is the phase associated with each Bloch wavefunction. The Bloch wavefunctions individually have arbitrary phase. The phase plays an important role in combining the Bloch wavefunctions into a Wannier function, finding the proper phase relationship to make the wavefunction maximally localized at each site [3].

#### 4.1.4 Pulsing vs adiabatic loading of the lattice

The lattice depth parameter  $V_0/4$ , for a range of values, can be well calibrated experimentally by pulsing on the lattice. Here, the word pulsing indicates that the lattice is turned on fully non-adiabatically, if not instantaneously, such that the original bare momentum state is projected onto the lattice eigenbasis, as shown

in Figure 4a. If the atoms start out stationary in the trap, the bare state in the momentum basis is simply

$$|\Psi_0\rangle = \begin{pmatrix} \vdots \\ 0 \\ 0 \\ 1 \\ 0 \\ 0 \\ \vdots \end{pmatrix}, \quad (4.20)$$

as depicted in Figure 4b.

Since the lattice eigenbasis is distinct from the bare one, instantaneously turning on the lattice will necessarily excite the atoms into a superposition of lattice eigenstates, each evolving with a different phase according to the eigenenergy while the lattice is on, as shown in Figure 4c. Then, when the lattice is snapped back off, the wavefunction is projected back into the bare basis, and the varying phase accumulation results in a beating of the different momentum orders, see Figure 4d. This can be calculated simply by using the time evolution operator

$$|\Psi(t)\rangle = e^{-iH_L t/\hbar} |\Psi_0\rangle. \quad (4.21)$$

By pulsing on the lattice for variable amounts of time  $t$ , we can obtain fractional populations in the different momentum states. Time-of-flight imaging captures the momentum distribution of the cloud, and the different entries of  $\Psi(t)$  in the momentum basis will thus appear as different clouds on the absorption image, as shown in Figure 3a. The fractional population in these clouds corresponds to a measurement of  $|a_j|^2$ . Typically for our values of the lattice depth  $V_0 < 10E_L$ , it is sufficient to simply count three central momentum orders,  $k = q, q \pm 2k_L$ . Then, we can fit Eq.

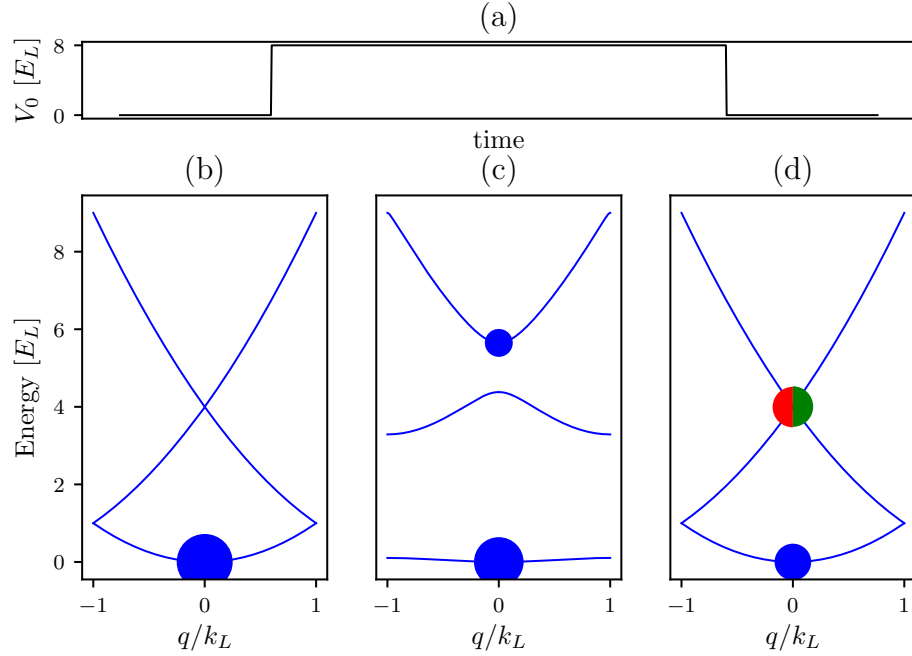


Figure 2: Lattice pulsing. (a) Lattice depth as a function of time during a pulsing experiment. The lattice is turned on instantaneously at  $t = 0$  and held on for a variable amount of time until being turned off instantaneously at a final time  $t = t_f$ . (b) Atomic population before  $t = 0$ . The dispersion relation is that of a free particle, and all of the atoms start out at  $q = 0$  in the lowest energy level. Here, the area of the dots is proportional to the fractional population in the energy state. (c) Atomic population after the lattice is turned on for a lattice depth of  $V_0 = 8.0 E_L$ . The energy spectrum now shows the lattice band structure, and some atomic population is projected onto the excited bands. (d) Atomic population after the lattice is snapped off at  $t_f = 150 \mu\text{s}$ . The wavefunction is projected back onto the bare states, with some fraction (blue circle) in the lowest band at  $k = 0$  and some fraction in the excited band, with equal population being projected onto the  $k = 2k_L$  (green) and  $k = -2k_L$  (red).

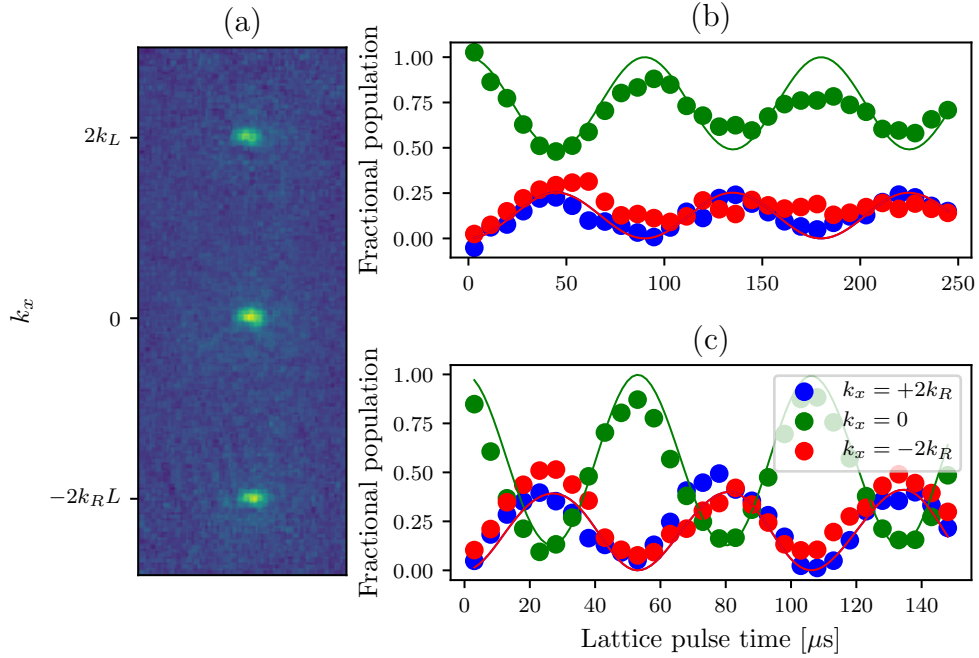


Figure 3: Lattice pulsing for calibration. (a) An example time-of-flight image from a pulsing experiment. The three different clouds are different momentum orders. (b) Fractional populations in the different momentum orders as a function of pulsing time at a low lattice power. Data is indicated by dots and best fit theory is represented by lines. The lattice depth from fit is  $V_0 = 5.57 \pm 0.07 E_L$ . (c) Fractional populations in the different momentum orders as a function of pulsing time at a higher lattice power. Data is indicated by dots and best fit theory is represented by lines. The lattice depth from fit is  $V_0 = 12.69 \pm 0.07 E_L$ .

4.21 to the data with fitting parameter  $V_0$ , thus deducing the lattice depth. Some examples of these pulsing experiments are presented in figure 3b,c.

In contrast to pulsing, adiabatic loading turns the lattice on slowly, such that the atomic wavefunction starting in the bare ground state can continuously adjust to remain in the ground state of the current Hamiltonian, without projecting onto any of the higher bands. This process is illustrated in Figure 4. The adiabatic timescale depends on the spacing between the ground and next excited band (or if starting in a different eigenstate, the nearest eigenstate). If the energy difference between the ground and first excited state is  $\Delta E$ , the timescale on which the lattice

is turned on must fulfill  $t \gg \hbar/\Delta E$ .

## 4.2 Raman and rf coupling

The second, 'synthetic' dimension in the effectively 2-D lattice is formed by the internal hyperfine states of the atoms, forming sites along a second dimension. To induce tunneling along the synthetic sites, analogous to lattice hopping between neighboring sites, we must engineer some coupling between them. There are two ways we induce this tunneling - with rf coupling, tuned to be directly resonant with the energy difference between the hyperfine levels, and with two-photon Raman coupling, tuned such that the energy difference between the two photons matches the hyperfine splitting. In this section we describe the hyperfine structure of  $^{87}\text{Rb}$ , derive the Hamiltonians for both rf and Raman coupled states, and show how the Raman and rf coupled states are measured and calibrated in the lab.

### 4.2.1 Hyperfine structure

Alkali atoms' energy levels can be understood as primarily the energy state of the single electron in the outer shell. Fine structure arises from different combinations of angular momenta, including orbital angular momentum of the outermost electron with respect to the nucleus  $\mathbf{L}$ , the electron spin  $\mathbf{S}$  and the nuclear spin  $\mathbf{I}$ . The total electron angular momentum is the combination of orbital and the spin angular momenta  $\mathbf{J} = \mathbf{L} + \mathbf{S}$ , and the quantum number can be any integer  $|L - S| \leq J \leq |L + S|$ . The ground state of  $^{87}\text{Rb}$ , in term notation  $^{2S+1}L_J$  is  $^2S_{1/2}$ , where  $S$  is orbital notation indicating  $L = 0$ . Since the total spin quantum number  $J = 1/2$ , this produces two possible spin projection quantum numbers,  $m_J = \pm 1/2$ .

There is also a contribution from the nuclear spin  $\mathbf{I}$ , resolvable at low magnetic fields, which gives rise to hyperfine structure of the states. For  $^{87}\text{Rb}$ ,  $I = 3/2$ . The



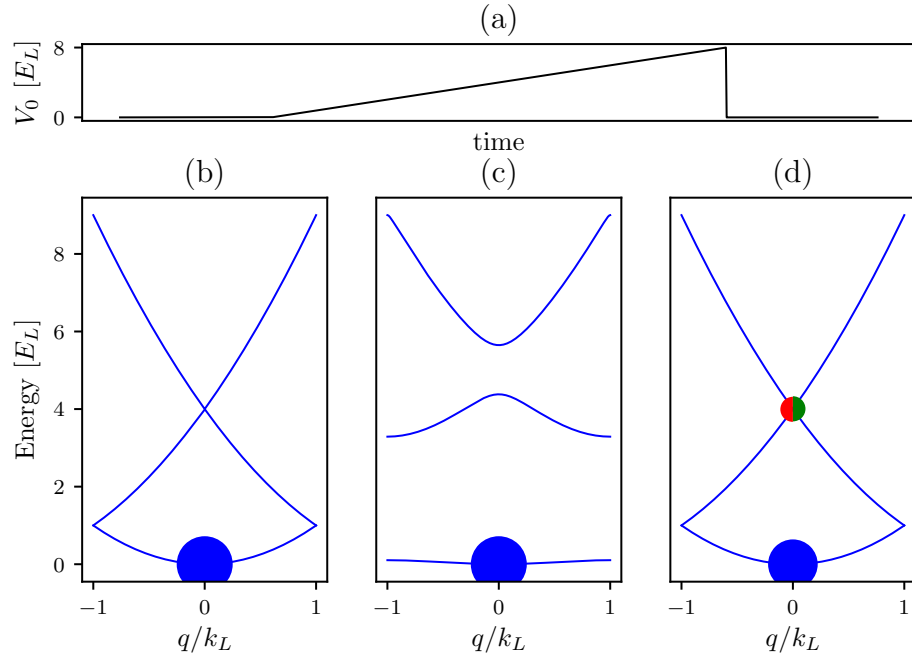


Figure 4: Adiabatic lattice loading. (a) Lattice depth as a function of time during adiabatic turn-on. The lattice is ramped on starting at  $t = 0$ , slowly increasing to a final lattice depth and turned off instantaneously at a final time  $t = t_f$ . (b) Atomic population before  $t = 0$ . All atoms are at  $k = 0$  in the lowest bare band. (c) Atomic population after the lattice is turned on adiabatically to a lattice depth of  $V_0 = 8.0 E_L$ . All atoms remain in the lowest band, but the band is no longer bare. (d) Atomic population after the lattice is snapped off. The wavefunction is projected back onto the bare states, with some fraction (blue circle) in the lowest band at  $k = 0$  and some fraction in the excited band, with equal population being projected onto the  $k = 2k_L$  (green) and  $k = -2k_L$  (red). Since the lowest lattice band is a superposition of bare bands, some atoms are excited to the higher bare bands.

total spin, including nuclear spin, is indicated by the quantum number  $F$ , and  $|J - I| \leq F \leq |J + I|$ . The interaction with the nuclear spin splits the ground state of  $^{87}\text{Rb}$  into two manifolds,  $F = 1$  and  $F = 2$ , with three hyperfine states in the  $F = 1$  manifold ( $m_F = 0, \pm 1$ ) and five hyperfine states in the  $F = 2$  manifold ( $m_F = 0, \pm 1, \pm 2$ ). These states couple to an external magnetic field  $B_z$  along some direction  $\mathbf{e}_z$  via the Hamiltonian  $H_B = \mu_B(g_J J_z + g_I I_z)B_z/\hbar$ . Here  $\mu_B$  is the Bohr magneton, and  $g_J$  and  $g_I$  are Lande g-factors. Since  $g_J \gg g_I$ , at high fields the nuclear spin interaction becomes small compared to the total energy shift, and the levels are grouped according to their  $m_J$  quantum number, as seen in Figure 5.

At low fields, however, the states are approximately linearly dependent on the  $m_F$  quantum number. The linear shift from the  $B = 0$  states is known as the linear Zeeman shift. In the intermediate regime, the correction to the linear shift can be expressed in terms of an energy correction to each hyperfine state  $\epsilon(B)|m_F|^2$ , known as the quadratic Zeeman shift. For the magnetic fields used in experiments described in this thesis, this correction is sufficient for describing the energy levels.

The form of the Hamiltonian in this regime for any value of  $F$  is given by

$$H_0 = H_{\text{KE}} + \hbar\omega_z \mathbf{F}_z + \hbar\epsilon \mathbf{F}_z^2, \quad (4.22)$$

where  $\hbar\omega_z = \mu_B g_F B_z/\hbar$ , and the kinetic energy Hamiltonian  $H_{\text{KE}} = \hbar^2 \vec{k}^2 / 2m\mathcal{I}$ , and  $\mathcal{I}$  is the identity matrix.

#### 4.2.2 Rf coupling Hamiltonian

For the  $F = 1$  manifold, there are three available spin states  $m_F = 0, \pm 1$ . There are many ways of introducing coupling terms between the different hyperfine states. Here, we will explain two methods: rf coupling and Raman coupling. Rf coupling is a radio-frequency oscillating magnetic field, in our case produced by a

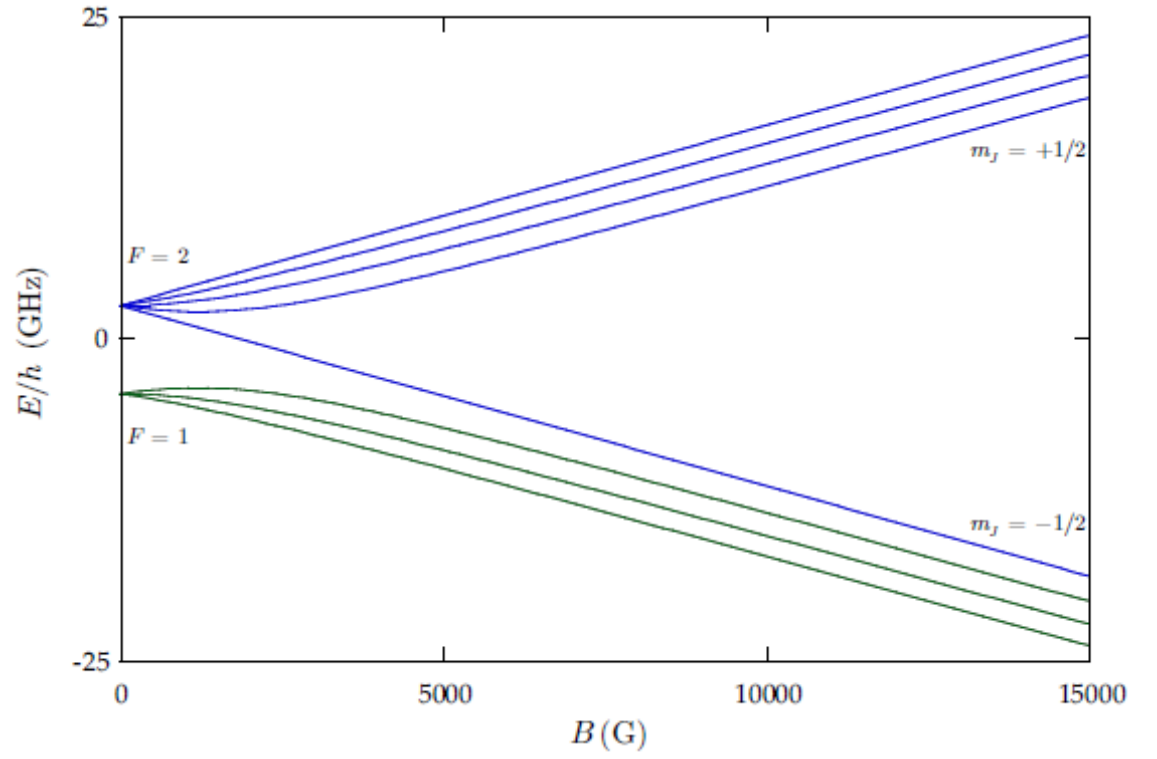


Figure 5: Energy structure of hyperfine states of the ground state of  $^{87}\text{Rb}$  as a function of external magnetic field strength in Gauss. Figure from ref. [4]

pair of circular coils in series side by side above the atoms (see [5]). Assuming the rf oscillating field is polarized along the  $\mathbf{e}_x$ , with the bias field along  $\mathbf{e}_z$ , the coupling Hamiltonian is given by  $H_{rf} = \mu_B g_F \vec{\mathbf{F}} \cdot \vec{\mathbf{B}} = \mu_B g_F \mathbf{F}_x B_x \cos(\omega t)$ , where  $2\pi\omega$  is the rf frequency. The schematic of this setup is shown in Figure 6. The eigenstates of the bare Hamiltonian  $H_0$  are the constituent  $m_F$  states. The eigenstates of the coupled Hamiltonian  $H_0 + H_{rf}(t)$  can be expressed as a linear superposition of the bare eigenstates  $\Psi(\vec{x}, t) = \sum_{m_F} c_{m_F}(t) \phi_{m_F}(\vec{x}) e^{-i\omega_{m_F} t}$ . The Hamiltonian in this basis can then be written as [?]

$$H_{\text{rf}} = H_{\text{KE}} + \hbar \begin{pmatrix} 0 & \Omega \cos(\omega t) e^{i\omega_z t} & 0 \\ \Omega \cos(\omega t) e^{-i\omega_z t} & 0 & \Omega \cos(\omega t) e^{i\omega_z t} \\ 0 & \Omega \cos(\omega t) e^{-i\omega_z t} & 0 \end{pmatrix}, \quad (4.23)$$

where  $\Omega$  is the Rabi frequency, proportional to  $B_x$ . We can then transfer into the rotating frame  $c'_{m_F} = e^{-im_F \delta t} c_{m_F}$ , where  $\delta = \omega_z - \omega$ . Then we apply the rotating wave approximation, that the fast oscillating terms average to zero over time scales of interest  $e^{2i\omega t} \approx 0$ , and obtain

$$H_{\text{rf}} = H_{\text{KE}} + \hbar \begin{pmatrix} \delta & \Omega/2 & 0 \\ \Omega/2 & -\epsilon & \Omega/2 \\ 0 & \Omega/2 & -\delta \end{pmatrix}, \quad (4.24)$$

or for any value of  $F$

$$H_{\text{rf}} = H_{\text{KE}} + \hbar \delta F_z + \hbar \epsilon F_z^2 + \Omega F_x / 2. \quad (4.25)$$

The band structure of this Hamiltonian can be seen in Figure 7, where we have diagonalized Eq. 4.24 for a range of momenta  $k_x$  (we have isolated  $k_x$  for comparison with Raman coupling, as will be seen in the next section). The parabolas are simply

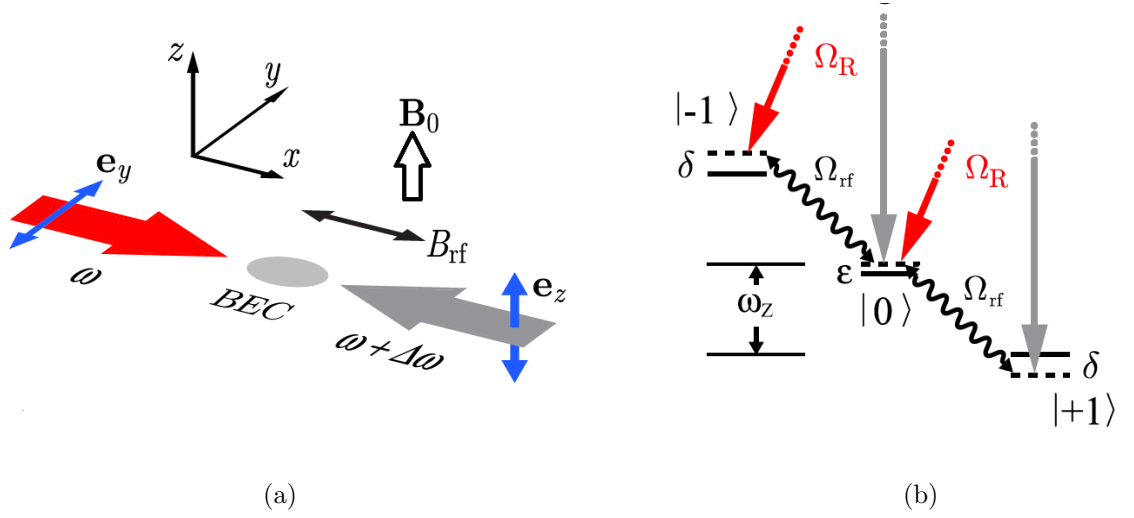


Figure 6: Raman and rf coupling schematic. (a) Beam geometry of the Raman beams and rf relative to the external field. The Raman beams have a frequency difference  $\Delta\omega$ , and are linearly polarized in perpendicular directions. (b) Level structure of both Raman and Rf coupling for hyperfine states of the  $F = 1$  manifold. The hyperfine splitting separates the levels by an energy  $\hbar\omega_z$ . The quadratic Zeeman shift  $\epsilon$  lowers the energy of the  $m_F = 0$  state, and the detuning  $\delta$  of either the Raman or the rf fields shifts the energies of the  $m_F = \pm 1$  states. Raman transitions are two-photon, exciting up to a virtual state and coming back down to an adjacent hyperfine state, with an accompanying momentum transfer. Rf couples adjacent hyperfine states directly. Figure taken from ref. [6]

the free particle dispersion relations along one dimension, with three bands arising from the three available spin states. It is convenient to define the magnetization of an eigenstate  $m = \sum_{m_F} m_F * p_{m_F}$ , where  $p_{m_F}$  is the fractional population in the  $m_F$  state. We have indicated the magnetization of the eigentate by coloring the eigenenergies, with  $m = -1$  in red,  $m = 0$  in green, and  $m = +1$  in blue. In Figure 7a, both the detuning and the coupling strength are zero. Therefore, there are simply three free particle dispersions, each exactly correlated with a particular spin state, the  $m_F = \pm 1$  are degenerate and the  $m_F = 0$  state is slightly offset by the quadratic shift  $\hbar\epsilon$ . In Figure 7c, the coupling strength is again zero, but the detuning has been turned on, lifting the degeneracy between the  $m_F = \pm 1$  states. Figure 7b,d shows the same conditions as a,c, respectively, but with the coupling strength turned on. In Figure 7b, where the detuning is zero and the quadratic shift is negligible compared to the coupling strength, all states average to a magnetization of zero—the  $m_F = \pm 1$  states are symmetrically populated. In Figure 7d, this symmetry is broken by the presence of a detuning.

### 4.3 Raman coupling Hamiltonian

The counter-propagating Raman beams, as seen in Figure 6, couple the same states as the rf. They do so via the vector light shift created by the pair of beams. The electric field due to the right going beam (red in Figure 6a) is  $\mathbf{E} = E_0 \exp(ik_R x - i\omega t) \mathbf{e}_y$ , where  $E_0$  is the amplitude of the electric field and  $\hbar k_R = h/\lambda_R = \hbar\omega/c$ . The electric field from the left going beam (gray in Figure 6b) is  $\mathbf{E} = E_0 \exp(-ik_R x - i(\omega + \Delta\omega)t) \mathbf{e}_z$ . This combines to give an effective field from the vector light shift [?]  $B_{\text{eff}} \propto \mathbf{E} \times \mathbf{E}^* \propto -E_0^2 \cos(2k_R x + \Delta\omega t) \mathbf{e}_x$ . Going through the same procedure as for the rf coupling case, including the transfer into the rotating frame and the rotating wave approximation, we obtain the same Hamiltonian in the basis of bare spin states  $|-1\rangle, |0\rangle, |1\rangle$  but with an extra phase factor:

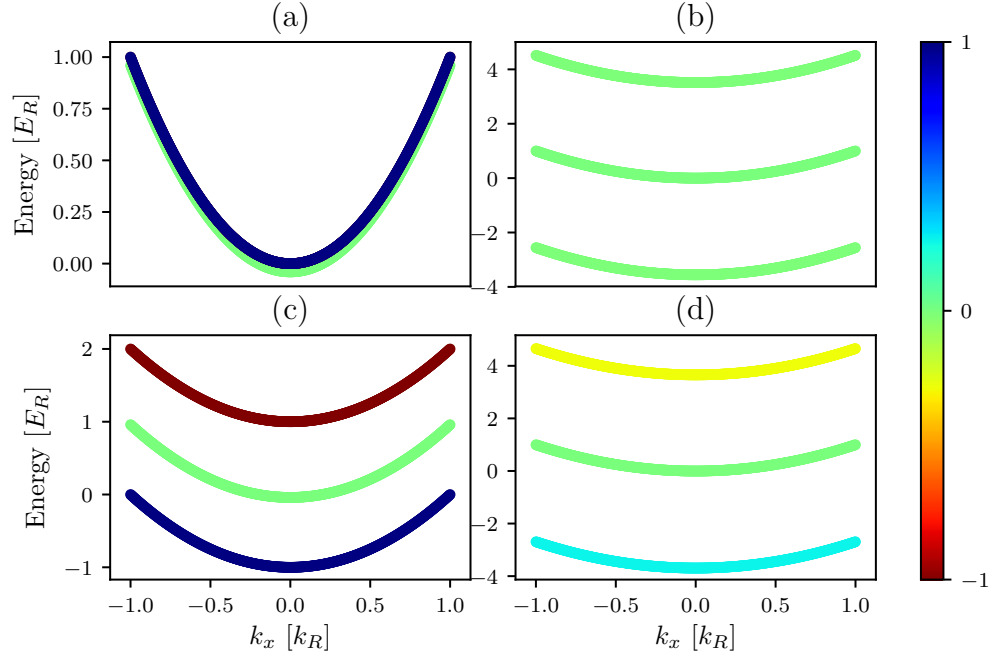


Figure 7: Band structure of the rf Hamiltonian, Eq. 4.24, in momentum space. For all plots, the quadratic Zeeman shift  $\hbar\epsilon = 0.04E_R$ , and the color represents magnetization, labeled by the colorbar. (a)  $\hbar\Omega = 0$ ,  $\hbar\delta = 0$ . No coupling or detuning is present, so the only separation between the bands is due to the quadratic shift  $\hbar\epsilon$ . (b)  $\hbar\Omega = 5.0E_R$ ,  $\hbar\delta = 0$ . (c)  $\hbar\Omega = 0$ ,  $\hbar\delta = 1.0E_R$ . Even though the coupling strength is zero, the bands are separated by the detuning. (d)  $\hbar\Omega = 5.0E_R$ ,  $\hbar\delta = 1.0E_R$ .

$$H_{\text{Raman}} = H_{\text{KE}} + \hbar \begin{pmatrix} \delta & \Omega/2e^{-i2k_R x} & 0 \\ \Omega/2e^{i2k_R x} & -\epsilon & \Omega/2e^{-i2k_R x} \\ 0 & \Omega/2e^{i2k_R x} & -\delta \end{pmatrix}, \quad (4.26)$$

where  $\delta = \omega_z - \Delta\omega$ .

This phase difference between the rf and Raman Hamiltonian has an intuitive physical explanation. In order to undergo a Raman transition, an atom first absorbs a photon from one beam, getting a momentum kick equal to the recoil momentum  $\hbar k_R$ . Then, to decay back down to an adjacent spin state, the undergoes stimulated emission into the field of the other (counter-propagating) beam, acquiring another recoil momentum kick in the same direction for a total of  $2\hbar k_R \mathbf{e}_x$ . Therefore, the Raman coupling Hamiltonian for  $F = 1$ , after transforming into the rotating frame and performing the rotating wave approximation, can be written in the same way as the rf Hamiltonian in Eq. 4.24 with the addition of a momentum kick—in real space, an aquired phase—of  $e^{i2k_R x}$ .

We can again make a basis transformation to get rid of this phase. Let us define  $|-1\rangle' = \exp(-2ik_R x)|-1\rangle = |k_x - 2k_R, -1\rangle$ ,  $|0\rangle' = |0\rangle = |k_x, 0\rangle$ ,  $|1\rangle' = \exp(2ik_R x)|1\rangle = |k_x + 2k_R, 1\rangle$ , where for third definition we went into the momentum basis and labelled the states by a combination of their momentum and spin state. Then, including the kinetic energy term along  $\mathbf{e}_x$  explicitly, we obtain the Hamiltonian in the new basis as:

$$H_{\text{Raman}} = H_{\text{KE}}^{(y,z)} + \begin{pmatrix} \frac{\hbar^2(k_x - 2k_R)^2}{2m} + \hbar\delta & \hbar\Omega/2 & 0 \\ \hbar\Omega/2 & \frac{\hbar^2 k_x^2}{2m} - \hbar\epsilon & \hbar\Omega/2 \\ 0 & \hbar\Omega/2 & \frac{\hbar^2(k_x + 2k_R)^2}{2m} - \hbar\delta \end{pmatrix}. \quad (4.27)$$

It is convenient to define the Raman recoil energy as  $E_R = \frac{\hbar^2 k_R^2}{2m}$ . The band structure of this Hamiltonian is shown in Figure 8, for several representative pa-



parameter values, with the magnetization labelled by the color. Figure 8a shows the band structure in the limit of zero coupling and zero detuning, but where we have already gone into the basis  $|k_x - 2k_R, -1\rangle, |k_x, 0\rangle, |k_x + 2k_R, 1\rangle$ ; therefore, the free particle parabola corresponding to the  $m_F = 1$  spin states is shifted to center on  $k_x = -2k_R$  and the  $m_F = -1$  parabola is shifted to center on  $k_x = 2k_R$ . As the coupling is turned on to  $\hbar\Omega = 1E_R$  in Figure 8b, the points where the parabolas cross become 'avoided crossings', separating into three bands where magnetization (and the underlying spin distribution) depends on the momentum  $k_x$ . As the coupling strength is turned up even further to  $\hbar\Omega = 5E_R$  in Figure 8c, the lowest band goes from having three minima, one corresponding to each original spin state, to only one minimum. This transition happens at  $\hbar\Omega = 4E_R$  [5]. In Figure 8d, we show the band structure again in the limit of zero coupling, but this time with a detuning of  $\hbar\delta = 1.0E_R$ . Note that the detuning tips the parabolas with respect to each other. Figure 8e shows the detuned system with coupling strength turned up to  $\hbar\Omega = 1E_R$ , still in the three minima regime but with avoided crossings creating three momentum and spin coupled bands. In Figure 8f, the detuned system is turned up to a coupling strength of  $\hbar\Omega = 5E_R$ , creating a single minimum, this time offset from  $k_x = 0$ .

We can write the general  $F$  version of the Raman coupled Hamiltonian in the basis  $|k_x + m_F * 2k_R, m_F\rangle$ , where  $-F \leq m_F \leq F$ , as:

$$H_{\text{Raman}} = H_{\text{KE}}^{(y,z)} + \hbar^2(k_x \mathcal{I} + 2k_R F_z)^2 / 2m + \hbar\delta F_z + \hbar\epsilon F_z^2 + \Omega F_x / 2. \quad (4.28)$$

### 4.3.1 Calibration of Raman and Rf dressed states

To calibrate the rf and Raman coupling strengths, we take a similar approach to the 1-D lattice calibration: start in a pure spin state, for example  $m_F = 0$ , and turn the coupling on non-adiabatically to induce Rabi oscillations between the

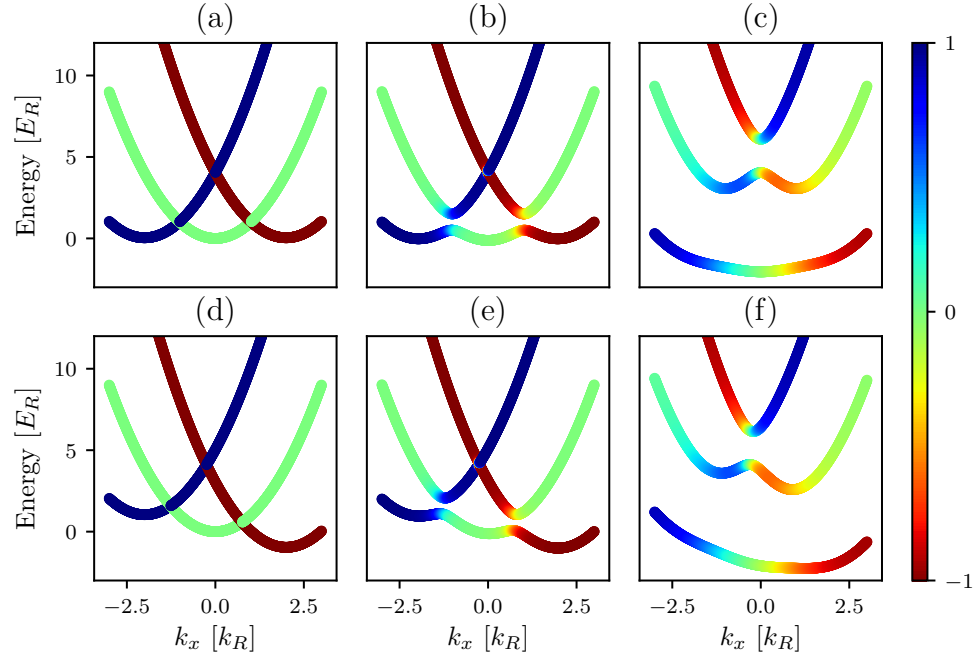


Figure 8: Band structure of the Raman Hamiltonian, Eq. ??, in momentum space. For all plots, the quadratic Zeeman shift  $\hbar\epsilon = 0.04E_R$ , and the color represents magnetization, labeled by the colorbar. (a)  $\hbar\Omega = 0$ ,  $\hbar\delta = 0$ . (b)  $\hbar\Omega = 1.0E_R$ ,  $\hbar\delta = 0$ . (c)  $\hbar\Omega = 5.0E_R$ ,  $\hbar\delta = 0$ . (d)  $\hbar\Omega = 0.0$ ,  $\hbar\delta = 1.0E_R$ . (e)  $\hbar\Omega = 1.0E_R$ ,  $\hbar\delta = 1.0E_R$ . (f)  $\hbar\Omega = 5.0E_R$ ,  $\hbar\delta = 1.0E_R$ .

coupled states. Then, during time-of-flight, apply a Stern-Gerlach gradient pulse to separate the spin components and observe the fractional populations in different spin states as a function of Rabi oscillation time.

Figure 9a,b shows example images obtained in time-of-flight when pulsing on an rf coupling field for atoms in the  $F = 1$  and  $F = 2$  manifold, respectively. The Stern-Gerlach gradient pulse separates the spin components along the horizontal axis in the images. The fractional population in each state can then be obtained by summing up the optical depth in each cloud and dividing by the total optical depth. Similarly, Figure 10a shows an example time-of-flight image obtained when pulsing on a Raman coupling field on an  $F = 1$  cloud initially in the  $m_F = 0$  spin state. Here, the spin states are separated along the horizontal axis by the same Stern-Gerlach pulse. In addition, the recoil momentum obtained when undergoing a Raman transition separates the different spin states along the vertical axis—parallel to the Raman beams along  $\mathbf{e}_x$ . The direction of the Stern-Gerlach gradient was chosen purposefully to be perpendicular to the Raman direction  $\mathbf{e}_x$  for easy separation of the two effects.

These population oscillations can then be fit for coupling strength  $\hbar\Omega$  and detuning  $\hbar\delta$ . Note that the quadratic Zeeman shift  $\hbar\epsilon$  is set by the strength of the bias field  $B_0$  and therefore often well known - we do not fit for this. The theoretic predictions are obtained by applying the time evolution operator  $U = \exp(-iH_{\text{Raman/rf}}t/\hbar)$  to an initial state  $\Psi$  in the appropriate basis. Figure 9c shows an example time series of rf pulsing in the  $F = 1$  manifold, starting in the  $m_F = 0$  state. The lines of best fit are overlayed on experimental data, extracting fit parameters  $\hbar\Omega = 0.863 \pm 0.004E_R$  and  $\hbar\delta = -0.198 \pm 0.007E_R$ . Figure 9d shows an example time series of rf pulsing in the  $F = 2$  manifold, starting in the  $m_F = -2$  state. Here, the extracted fit parameters were  $\hbar\Omega = 1.000 \pm 0.002E_R$  and  $\hbar\delta = -0.061 \pm 0.001E_R$ .

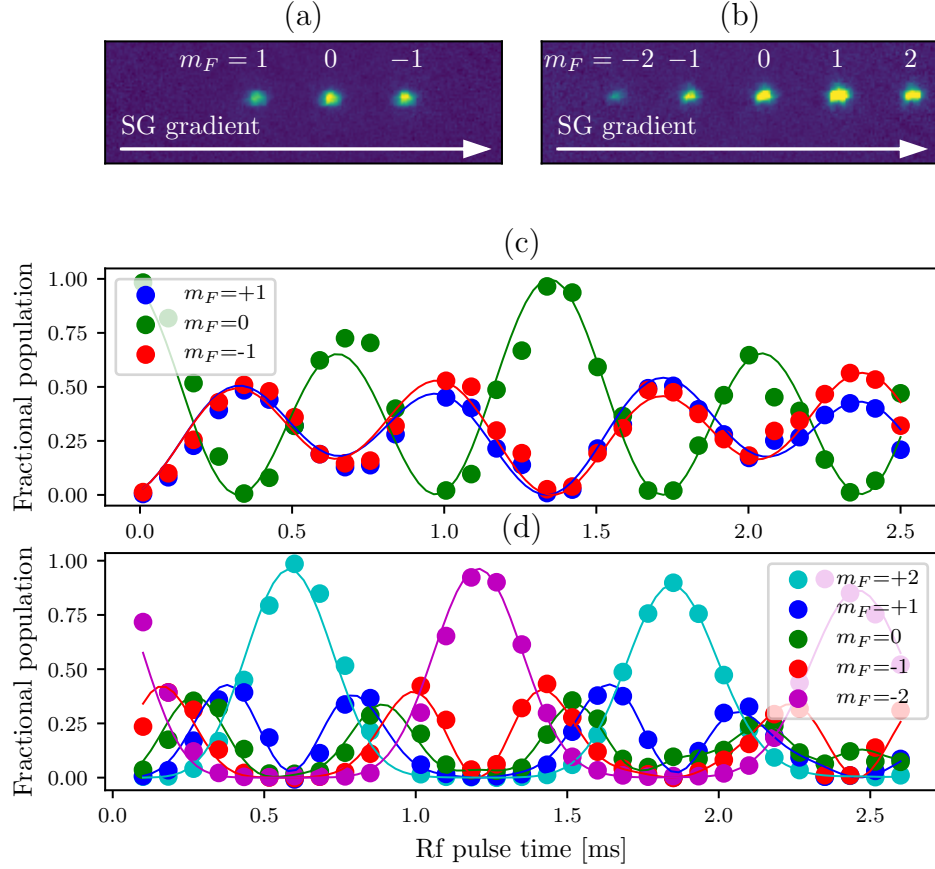


Figure 9: Pulsing on rf coupling. (a) Example time-of-flight image during an rf pulsing experiment in the  $F = 1$  manifold. Spin states are separated via a Stern-Gerlach pulse along the horizontal direction. (b) Example time-of-flight image during an rf pulsing experiment in the  $F = 2$  manifold. Here, 5 spin components are present. (c) Pulsing experiment in the  $F = 1$  manifold. Dots represent fractional populations in different spin states measured from time-of-flight images, and lines represent best fit theory curves. Fitted parameters are  $\hbar\Omega = 0.863 \pm 0.004E_R$ ,  $\hbar\delta = -0.198 \pm 0.007E_R$ . (d) Pulsing experiment in the  $F = 2$  manifold. Dots represent fractional populations in different spin states measured from time-of-flight images, and lines represent best fit theory curves. Fitted parameters are  $\hbar\Omega = 1.000 \pm 0.002E_R$ ,  $\hbar\delta = -0.061 \pm 0.001E_R$ .  $\hbar\epsilon = 0.038E_R$  for all panels.

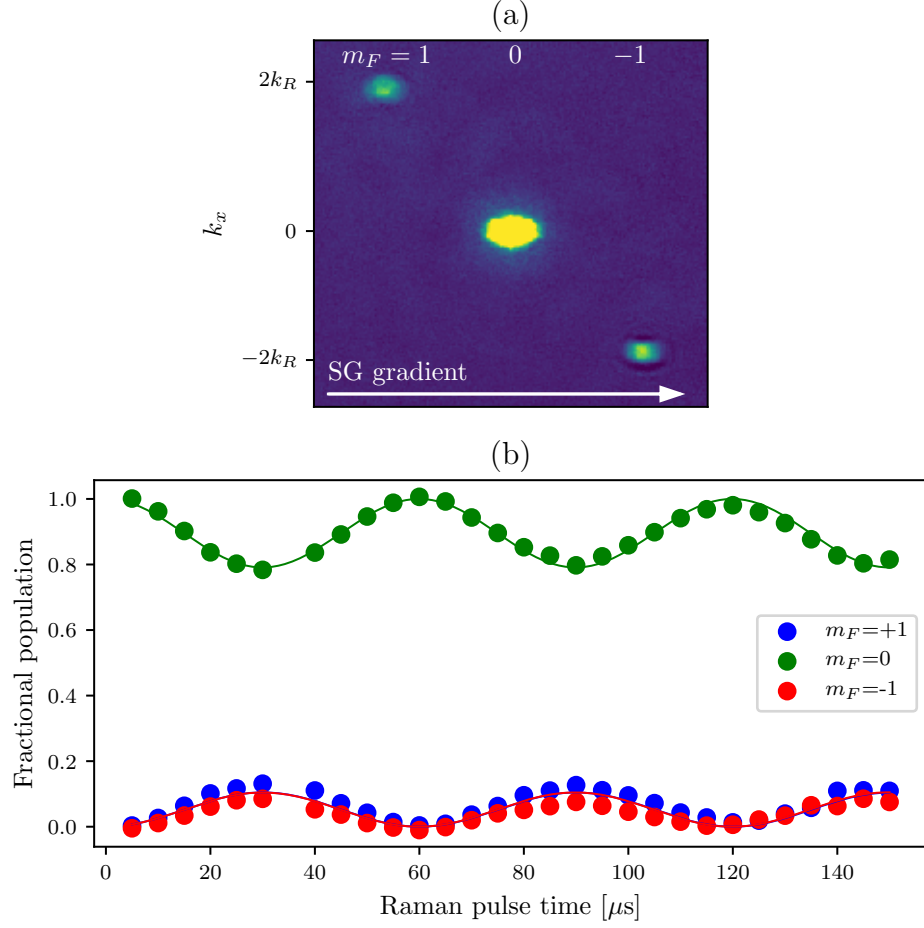


Figure 10: Pulsing on Raman coupling. (a) Example time-of-flight image during a Raman pulsing experiment in the  $F = 1$  manifold. A Stern-Gerlach pulse during time-of-flight separates different spin components along the horizontal direction, and different momentum orders fly apart along the vertical direction. (b) Fractional population in different spin states during a Raman pulsing experiment as a function of time. Dots represent data and lines represent a best fit from theory. The fitted parameters are  $\hbar\Omega = 1.47 \pm 0.01E_R$ ,  $\hbar\delta = 0.004 \pm 0.024E_R$ . The quadratic Zeeman shift was  $\hbar\epsilon = 0.038E_R$ .

Figure 10b shows an example time series of Raman pulsing in the  $F = 1$  manifold, starting in the  $m_F = 0$  state, with fitted parameters  $\hbar\Omega = 1.47 \pm 0.01E_R$  and  $\hbar\delta = 0.004 \pm 0.024E_R$ . Note that although the coupling strength is almost double the rf coupling strength in Figure 9c, the contrast (peak to peak oscillation of the fractional population in, say, the  $m_F = 0$  state) is much lower in the Raman data than in the rf. This is a direct consequence of the recoil momentum transfer, and can be understood by looking at the band structure. For rf, the coupled bands at initial momentum  $k_x = 0$  are separated by the coupling strength, see Figure ??b. For Raman, even at zero coupling strength, due to the shifting of the parabolas by  $2k_R$ , and  $k_x = 0$  the higher bands are  $\hbar^2(2k_R)^2/2m = 4E_R$  separated from the lower bands. Therefore, the energy difference is larger and the fraction in the excited band will be lower, leading to lower contrast.

## 4.4 High effective magnetic fields via synthetic dimensions

In condensed matter, 2-D systems in high fields have proved to be of great technological use and scientific interest. The integer quantum Hall effect (IQHE) [?], with its quantized Hall resistance, had given rise to an ultra-precise standard for resistivity. It was also the

### 4.4.1 Synthetic dimensions

Figure: Schematic of beams,  $F = 1$  and  $F = 2$  dots with phases

par1: Explain setup

par2: Aharonov-Bohm phase

par3: Explanation of phases in Syn. dim.

par4: Effective field strength in terms of  $\phi_{AB}$

#### 4.4.2 Synthetic dimensions Hamiltonian

Figure: Band structure,  $F=1$  and  $F=2$ , with and without Raman coupling

par1: Write out full Hamiltonian

par2: Talk about band structure, periodic and spin dependent

par3: How we calibrate the synthetic dimensions system by pulsing

Figure: example TOF images, pulsing experiments for  $F=1$  and  $F=2$

par4: Write out tight binding version, explain how closely it applies. Figure: fits for effective tunneling amplitudes?

#### 4.4.3 Eigenstates of the synthetic 2-D lattice

par1: 'Edge' and 'bulk' states of electrons in a magnetic field

par2: Explain loading procedure for adiabatic states

par3: Explain figure, magnetic length

#### 4.4.4 Observation of skipping orbits

par1: Skipping orbits in 2-D electrons in a magnetic fields

par2: Experimental sequence for skipping orbits measurement

par3: How position is calculated from integrating velocity as a function of time. Explain figure

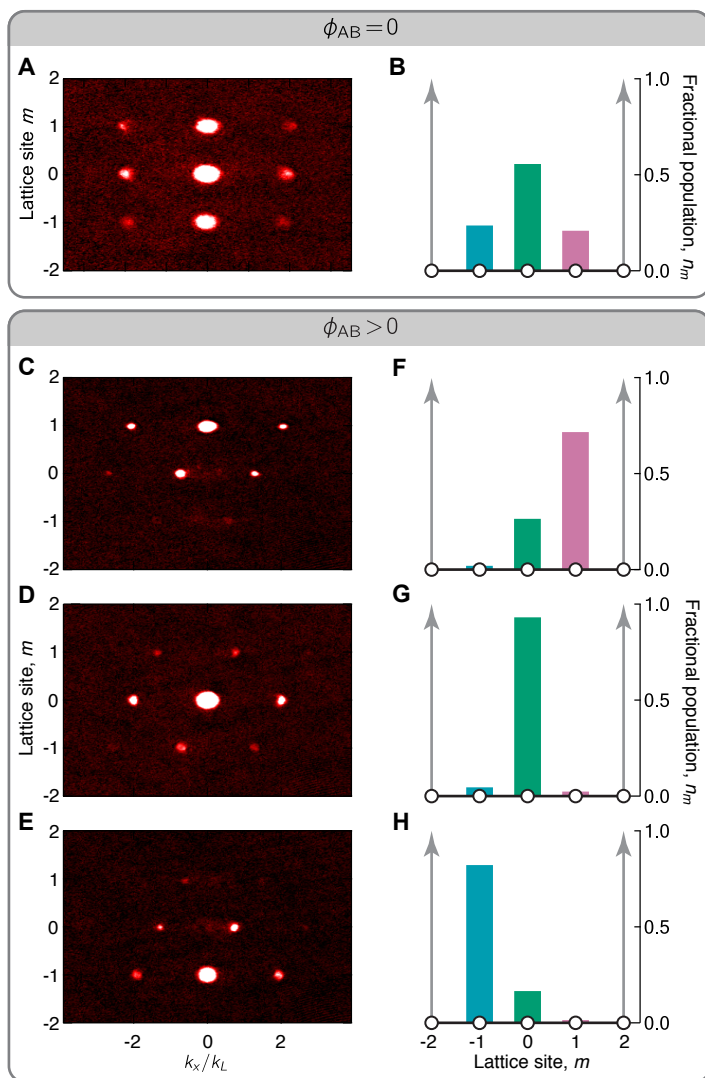


Figure 11:



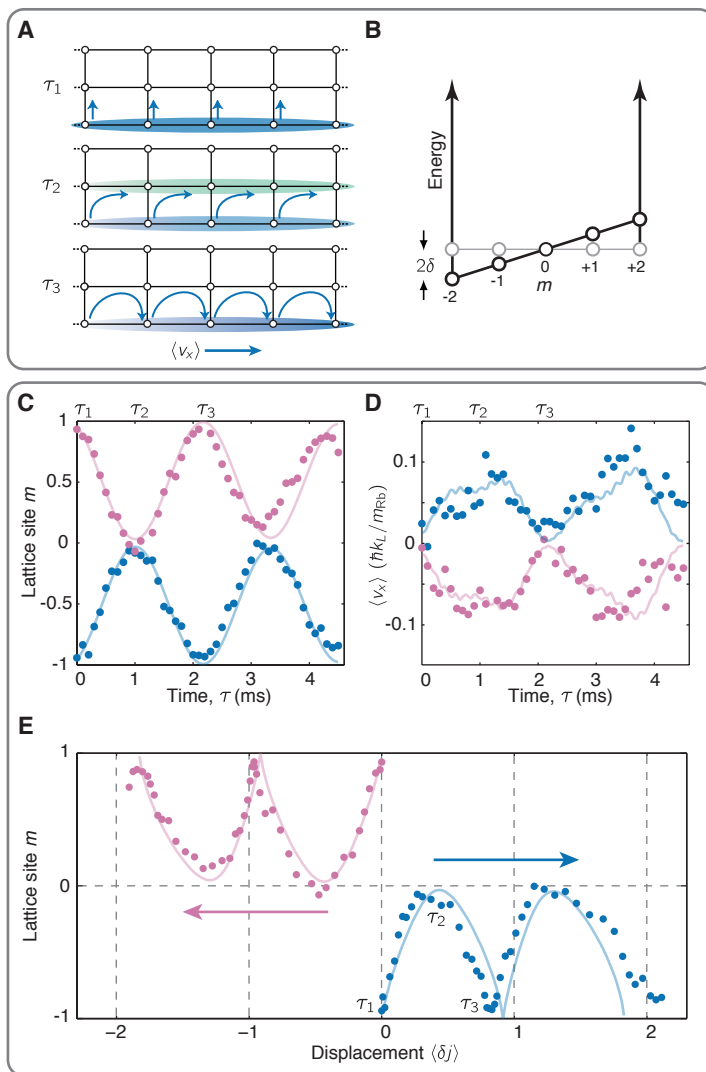


Figure 12:

## Bibliography

- [1] B. K. Stuhl, H.-I. Lu, L. M. Ayccock, D. Genkina, and I. B. Spielman. Visualizing edge states with an atomic bose gas in the quantum hall regime. *Science*, 349(6255):1514–, Sep 2015.
- [2] N.W. Ashcroft and N.D. Mermin. *Solid State Physics*. Saunders College, Philadelphia, 1976.
- [3] Nicola Marzari, Arash A. Mostofi, Jonathan R. Yates, Ivo Souza, and David Vanderbilt. Maximally localized wannier functions: Theory and applications. *Rev. Mod. Phys.*, 84:1419–1475, Oct 2012.
- [4] Daniel Adam Steck. Rubidium 87 d line data. Available online, <http://steck.us/alkalidata>, January 2015. revision 2.1.5.
- [5] Karina Jimenez-Garcia. *Artificial Gauge Fields for Ultracold Neutral Atoms*. PhD thesis, Joint Quantum Institute, National Institute of Standards and Technology, and the University of Maryland, 2012.
- [6] K. Jiménez-García, L. J. LeBlanc, R. A. Williams, M. C. Beeler, A. R. Perry, and I. B. Spielman. Peierls substitution in an engineered lattice potential. *Phys. Rev. Lett.*, 108:225303, May 2012.